Transitions between Taylor vortices and spirals via wavy Taylor vortices and wavy spirals

Ch Hoffmann[1], S Altmeyer, A Pinter and M Lücke

Institut für Theoretische Physik, Universität des Saarlandes,
D-66123 Saarbrücken, Germany
E-mail: chhof@lusi.uni-sb.de

Abstract. We present numerical simulations of closed wavy Taylor vortices and of helicoidal wavy spirals in the Taylor–Couette system. These wavy structures appearing via a secondary bifurcation out of Taylor vortex flow and out of spiral vortex flow, respectively, mediate transitions between Taylor and spiral vortices and vice versa. Structure, dynamics, stability and bifurcation behaviour are investigated in quantitative detail as a function of Reynolds numbers and wave numbers for counter-rotating as well as corotating cylinders. These results are obtained by solving the Navier–Stokes equations subject to axial periodicity for a radius ratio $\eta = 0.5$ with a combination of a finite differences method and a Galerkin method.

[1] Author to whom any correspondence should be addressed.

IOP Institute of Physics   Φ DEUTSCHE PHYSIKALISCHE GESELLSCHAFT

Contents

1. Introduction

This paper elucidates in quantitative detail how rotationally symmetric, stationary Taylor vortices in the Taylor–Couette system [1] are transformed into helicoidal, propagating spiral vortices and vice versa. Such transitions that are mediated by wavy-like structures have partially been predicted theoretically but have not yet been investigated extensively. Here we determine in detail how the solution branches of Taylor vortex flow (TVF) and spiral vortex flow (SPI) are connected via intermediate stable solutions, how the spatiotemporal properties change along the connections, how the stability is transferred between the branches, and where and what kind of transients occur.

Several theoretical and experimental investigations concern the interaction between TVF, SPI and a variety of different wavy solutions [2]–[9]. Here, we focus on wavy vortex flow (WVF) and on wavy spiral vortex flow (wSPI), which play, besides the so-called ribbons (RIB) [10, 11], a dominant role in the transitions between TVF and SPI. The phrase WVF is used in the literature to describe a state of 'wavy Taylor vortex flow' (wTVF) in which the former Taylor vortices are azimuthally modulated but remain toroidally closed into themselves [1]. For the sake of clarity we use the abbreviation wTVF. This flow state appears via a secondary, non-hysteretic forward bifurcation out of TVF [4, 5]. In the majority of publications the wTVF solution branch has been seen to return to the TVF branch or to undergo higher order bifurcations [5], [7]–[9], [12, 13] at larger driving.

On the other hand, toroidally closed TVF appears via a primary stationary bifurcation out of the rotationally symmetric, axially homogeneous basic circular Couette flow (CCF). Also the two axially symmetry degenerated oscillatory SPI states with left or right winding helicoidal

vortices [14] appear via primary bifurcations out of CCF in a symmetric Hopf bifurcation together with the RIB state. The latter can be seen as a nonlinear superposition of the two oppositely propagating SPI to an axially standing wave. Typically, RIB are unstable close to onset but can become stable later on under certain conditions [15]. The stability of TVF and SPI at onset is regulated by the order of their appearance upon increasing the inner cylinder's rotation rate Ω_1: the first (second) solution to bifurcate out of CCF is stable (unstable). However, the second, unstable solution can become stable at larger Ω_1. Which state bifurcates first depends on the outer cylinder rotation speed [1].

Besides parameter regions with monostability of TVF and SPI, one also observes regions with bistability of the two states [14]. When moving a control parameter out of this region, one solution loses its stability and the system undergoes a transition to the remaining stable state, i.e. from TVF to SPI or vice versa [14]. Bifurcation theoretical considerations and symmetry arguments [2, 3] as well as amplitude expansion techniques in [4] suggest that the solution branch of stable TVF is connected to unstable RIB via stable wTVF. In [2] a 'jump bifurcation' from the end of the stable wTVF branch to the stable SPI branch is expected. Such a behaviour has indeed been observed in our numerical calculations and it also seems to have been found in experiments by Tagg *et al* [6][2].

Golubitsky and Langford [3] presented qualitative bifurcation diagrams for a wide range of radius ratios $0.43 < \eta < 0.98$ showing that some properties (forward or backward bifurcation, stability changes, etc) strongly depend on η. The investigations of [2]–[4] further suggest the existence of a branch of wSPI that are sometimes also called modulated spirals. They bifurcate out of SPI but it was not possible to track this branch or to connect it to another solution. We found that these wSPI mediate the transition from SPI to TVF. Indeed, the symmetry considerations in [3] suggest a connection from SPI to unstable RIB via wSPI. Iooss' analysis [4] gives good guidance for the investigation of wSPI and wTVF.

This paper is roughly subdivided into three parts. After an introduction to the system and numerical methods in section 2, section 3 represents the essential part. It deals with the bifurcation behaviour of wTVF and wSPI which mediate the transition between the well-known TVF and SPI. Section 4 elucidates some further properties of these structures and explains the necessary topological and symmetry transformations that accompany the transition. All modes that are significant for the respective pure structures (TVF or SPI) are also excited in the spectra of the relaxed and stable wavy structures. However, they can also be observed in the transient solutions of the Navier–Stokes equations (NSE). The spatiotemporal behaviour of these transients is presented in section 5. The final section 6 summarizes our main findings.

2. System and theoretical description

We report the results obtained numerically for a Taylor–Couette system with co- and counter-rotating cylinders, fixed radius ratio $\eta = r_1/r_2 = 0.5$, no-slip boundary conditions at the cylinder surfaces and axial periodic boundary conditions determining the axial wave number k. The fluid in the annulus between the cylinders (gap width $d = r_2 - r_1$) is considered to be isothermal and incompressible with kinematic viscosity ν.

Cylindrical coordinates r, φ and z are used to decompose the velocity field into a radial component u, an azimuthal one v, and an axial one w:

$$\mathbf{u} = u\,\mathbf{e}_r + v\,\mathbf{e}_\varphi + w\,\mathbf{e}_z. \tag{1}$$

---

[2] Experiments cited in [3] as [1988] on p 508.

The system is governed by the NSE

$$\partial_t \mathbf{u} = \nabla^2 \mathbf{u} - (\mathbf{u} \cdot \nabla)\mathbf{u} - \nabla p. \tag{2}$$

Here, lengths are scaled by the gap width d and times by the radial diffusion time d^2/ν for momentum across the gap, and the pressure p is scaled by $\rho \nu^2/d^2$. The Reynolds numbers

$$R_1 = r_1 \Omega_1 d/\nu, \quad R_2 = r_2 \Omega_2 d/\nu \tag{3}$$

enter into the boundary conditions for ν. R_1 and R_2 are just the reduced azimuthal velocities of the fluid at the cylinder surfaces; Ω_1 and Ω_2 are the respective angular velocities of the cylinders.

2.1. Numerical methods

Results in this paper were obtained by two different numerical methods. First, the classical MAC code that we already presented in [14, 16] uses a Galerkin expansion (G) in one dimension φ as well as finite differences (D) in three dimensions r, z and t which are of first-order forward differences in time and second-order centered differences in space. In the following, we abbreviate this code as 'G1D3'. Additionally, we used a new 'G2D2' code with Galerkin expansion in two dimensions, φ and z, and finite differences of second order in r and of first order in t.

$$f(r, \varphi, z, t) = \sum_{m=-m_{\max}}^{m_{\max}} \sum_{n=-n_{\max}}^{n_{\max}} f_{m,n}(r, t) \, e^{i(m\varphi + nkz)}, \quad f \in \{u, v, w, p\}. \tag{4}$$

Here, $f_{m,n}(r, t)$ are the amplitudes of the mth azimuthal and the nth axial mode. Their variation in the two variables r and t is determined using finite differences. We checked that $m_{\max} = n_{\max} = 4$ provided sufficient accuracy, cf appendix A for more details.

Note that the decomposition (4) of the velocity fields allows one to impose restrictions and conditions on the modes $m \in \{-m_{\max} \ldots m_{\max}\}$, $n \in \{-n_{\max} \ldots n_{\max}\}$, e.g. to enforce certain symmetry conditions during the numerical calculations by suppressing those modes that do not belong to mode subspaces being of interest.

2.2. Amplitude equations

Here, we briefly mention results that pertain to amplitude equation approaches. Iooss *et al* [4] determined the phase diagram for wTVF. Furthermore, in [11] the bifurcation behaviour of wTVF and wSPI was investigated via amplitude equations near the bicritical point within a three-mode model. Therein appear the two critical SPI modes of a left-handed SPI (L-SPI) $A \equiv (m, n) = (1, 1)$ and of a right-handed SPI (R-SPI) $B \equiv (1, -1)$ together with the critical TVF mode $C \equiv (0, 1)$:

$$
\begin{aligned}
\dot{A} &= A \, F(|A|^2, |B|^2, |C|^2) + \mathrm{i} q_1 \, B \, C \, C, \\
\dot{B} &= B \, G(|A|^2, |B|^2, |C|^2) + \mathrm{i} q_1 \, A \, \bar{C} \, \bar{C}, \\
\dot{C} &= C \, H(|A|^2, |B|^2, |C|^2) + q_0 \, A \, \bar{B} \, \bar{C}.
\end{aligned}
\tag{5}
$$

Here, the overbar denotes complex conjugation. The coupling constants q_0, q_1 are real. The action of these coupling terms is shown in the figure below.
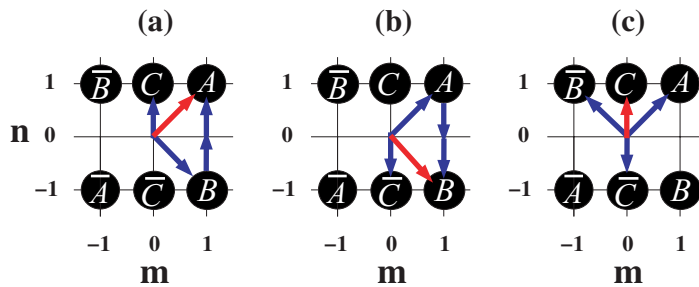
Invariance under axial translation and reflection of the Taylor–Couette system imposes restrictions on the otherwise arbitrary complex functions F, G, H. Thus, equation (5) has to be invariant under the operation $(A, B, C) \leftrightarrow (B, A, \bar{C})$, which is caused by the symmetry operation $z \to -z$. Within the limitations of such a model, it was shown that the wTVF branch connects the stable TVF with the unstable RIB solution. The latter then destabilizes against SPI. The investigations [11] suggest the existence of wSPI connecting the stable SPI with the unstable RIB branch. We are not aware of any experimental or further theoretical investigations of wSPI.

Golubitsky *et al* [3] investigated the isotropy subgroups and their relationships. Their results give reason to expect a stable branch of wSPI connecting SPI and RIB. The following figure shows the possible transitions between CCF, TVF, SPI, RIB, wTVF and wSPI.
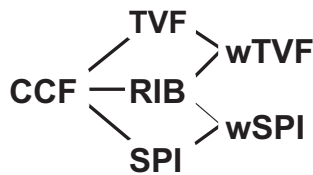
The transition from wSPI to RIB was not yet observed, so we indicated that by a thinner line. Another branch of so-called twisted vortices connecting TVF and RIB is described in the literature [2, 3] but we do not investigate it in this paper.

The following figure summarizes the content of the above figure and suggests transitions from SPI to TVF and vice versa via

$$\text{TVF} \underset{\leftarrow - - \rightarrow}{\overset{\text{wTVF}}{\rightleftarrows}} \text{RIB} \underset{\text{wSPI}}{\overset{\leftarrow - - \rightarrow}{\rightleftarrows}} \text{SPI}.$$

3. Bifurcation behaviour and phase diagrams

Here, we present bifurcation properties of TVF, SPI, RIB and of the connection branches of wTVF and wSPI as a function of R_1 and of wavenumber k and, furthermore, various planar and three-dimensional phase diagrams in (k, R_2, R_1) parameter space.

3.1. Bifurcation behaviour as a function of R_1

Figure 1 illustrates the stable (solid lines with closed symbols) and unstable (dashed lines with open symbols) bifurcation branches of TVF (blue circles), L-SPI (orange triangles), RIB (green lozenges), wTVF (black squares) and wSPI (black lozenges) versus R_1 at two fixed values of R_2 that are indicated by the arrows (a) and (b), respectively, in the phase diagram of figure 3.
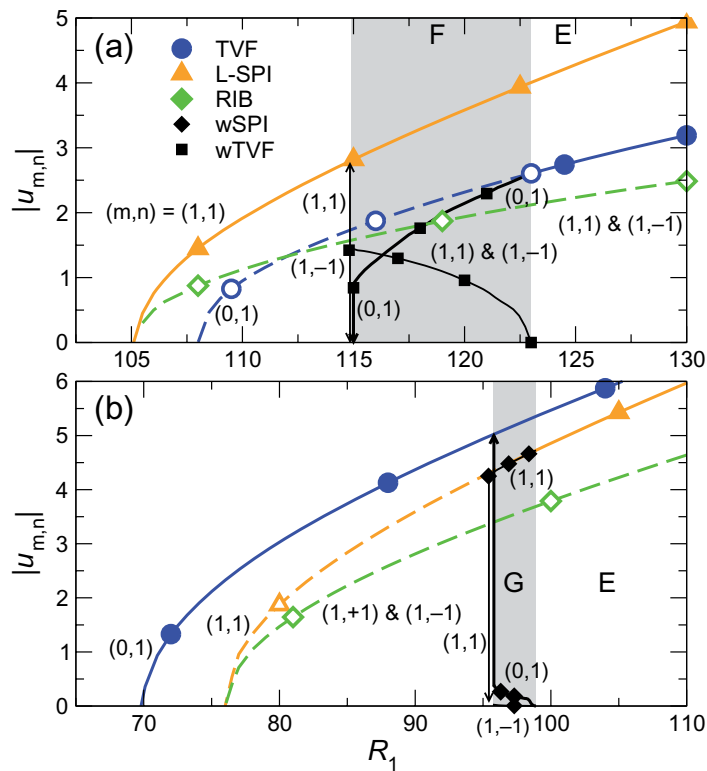
Figure 1. Bifurcation diagrams for different vortex structures versus R_1 for (a) $R_2 = -100$ and (b) $R_2 = -25$ (cf arrows in figure 3). Full (dashed) lines with filled (open) symbols refer to stable (unstable) solutions. Shown are the dominant radial flow field amplitudes $|u_{m,n}|$ at mid-gap for TVF $(m, n) = (0, 1)$, L-SPI $(m, n) = (1, 1)$, RIB $(|u_{1,1}| = |u_{1,-1}|)$, wTVF, and wSPI. The two wavy solutions are characterized by $u_{0,1} \neq 0$ and $u_{1,\pm 1} \neq 0$ while $u_{0,1}^{SPI} = 0 = u_{1,\pm 1}^{TVF}$. The amplitude of $(1, -1)$ of wSPI is very small and therefore cannot be distinguished from the abscissa in this plot. The bifurcation branches connecting to an R-SPI $(m, n) = (1, -1)$ that are identical due to mirror symmetry are not shown here for the sake of visibility. Further control parameters are $\eta = 0.5$ and $k = 3.927$. Here and in the other figures, the symbols primarily distinguish different structures. Calculations were typically done for many more parameters than the symbol locations.

3.1.1. Wavy Taylor vortices. We start our discussion of the bifurcation diagrams in figure 1(a) with a stable TVF state in region E. Upon decreasing R_1, TVF remains stable until R_1 reaches the grey coloured region F. There, two modes $(1, 1)$ and $(1, -1)$ emerge with exactly the same amplitude when stable wTVF (black squares) that is characterized by the three modes $(0, 1)$, $(1, 1)$ and $(1, -1)$ bifurcates secondarily out of the TVF. The latter loses stability to wTVF there. When decreasing R_1 further, the amplitude ratio $|u_{1,\pm 1}/u_{0,1}|$ increases and the modulation amplitude, i.e. the waviness of wTVF, is getting stronger and stronger.

Obviously, the $(1, 1)$ and $(1, -1)$ amplitudes of the wTVF state approach the unstable RIB branch. Because the system is unable to stay in the RIB solution, the $m = 0$ and one of the $m = 1$ amplitudes ($u_{1,-1}$ in this case) vanish at the left boundary of region F, whereas the amplitude
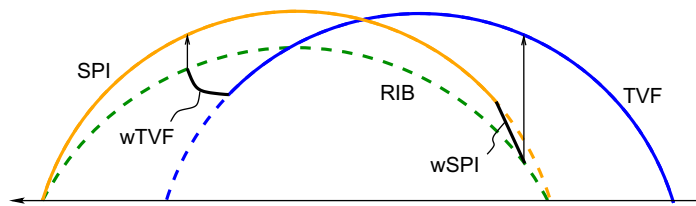
Figure 2. Schematic bifurcation diagram for a suitably chosen control parameter containing the results of figures 1 and 3. Stable (unstable) solutions are displayed as solid (dashed) lines. Thin arrows indicate the transients corresponding to the 'jump bifurcation' mentioned in [2].

of the remaining $m = 1$ mode (here $u_{1,1}$) jumps up to the dominant mode of the only remaining stable solution, the pure SPI (here L-SPI) structure (orange line with triangles). The pure SPI state is stable in the whole parameter range displayed in figure 1(a). Thus, SPI exist bistably with TVF in region E and bistably with wTVF in region F.

Note that for the sake of visibility, we presented only one of the two SPI branches in the figures, namely the L-SPI. The connection from TVF to the R-SPI branch via the RIB state looks exactly the same in the absence of symmetry breaking effects.

3.1.2. Wavy spiral vortices. Figure 1(b) displays the bifurcation behaviour for $R_2 = -25$ where wSPI appear. Consider first a stable SPI state (here an L-SPI identified by the dominant $(1, 1)$ mode) in region E. This solution loses its stability at the right boundary of region G where two further modes, $(0, 1)$ and $(1, -1)$, arise. $(1, 1)$ and $(1, -1)$ interact nonlinearly and generate a $(0, 2)$ mode which, however, has a significantly smaller amplitude than the $(0, 1)$ mode. With decreasing R_1, $(0, 1)$ as well as $(1, -1)$ increase monotonically, whereas the $(1, 1)$ mode decreases and seems to indicate an approach to the unstable RIB branch. But as in the case of figure 1(a), the system cannot develop the RIB state and all modes disappear at the left boundary of region G except $(0, 1)$ which jumps up to the stable TVF solution. Thus, TVF and wSPI exist bistably in region G.

For the parameters that we have chosen here, the $(1, 1)$ and $(1, -1)$ amplitudes of the wSPI state differ significantly. Furthermore, the amplitudes of the respective $(1, 1)$ modes belonging to the pure L-SPI and to the wSPI structure are almost identical, whereas the amplitude of the $(1, -1)$ mode in the wSPI solution is very small. However, this is not always the case. In fact, we found wSPI solutions with a more moderate mode ratio for other control parameters that are not discussed in this paper.

At the left borders of regions F and G in figure 1, the amplitudes of the respective modes of wTVF and wSPI show a significant jump. We tried to stabilize these solutions to the left of the grey coloured regions by enforcing symmetry conditions which are consistent with wavy solutions and not with SPI. But this always led to a stabilization of the RIB solution. So, we could not find with these mode restrictions the expected branches of unstable wSPI and wTVF at R_1 to the left of regions F and G and thus terminated our search.

Figure 2 contains the results of section 3.1 in a *schematic* bifurcation diagram with a suitable control parameter, say, e.g. R_2. Note again that the branches of wTVF and wSPI do not end exactly in the RIB branch due to the instability of the latter. The transients from unstable RIB to TVF and SPI, respectively, are indicated by thin arrows.
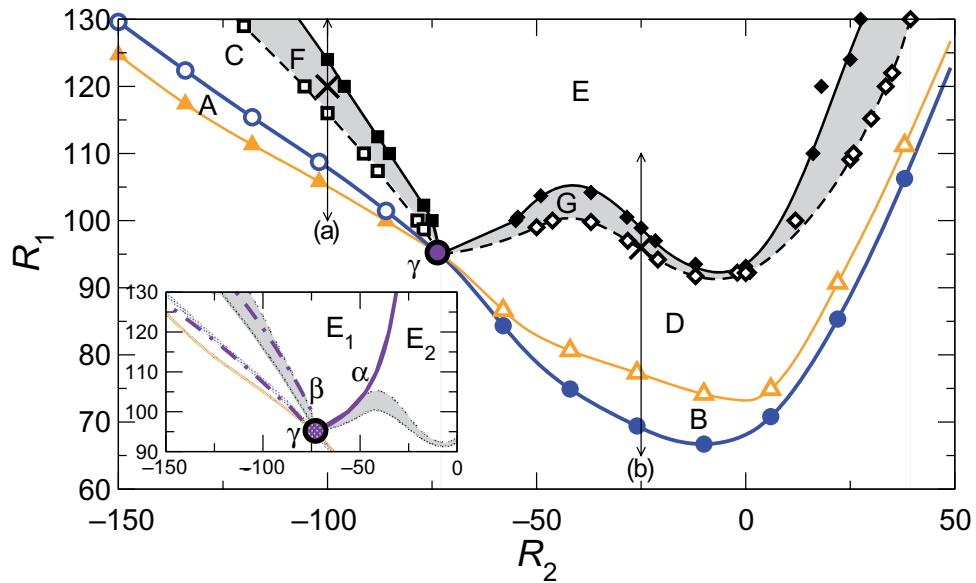
Figure 3. Phase diagram for TVF, SPI, wTVF, and wSPI for $\eta = 0.5$ and $k = 3.927$.

Region	A	B	C	D	E	F	G
TVF	–	s	u	s	s	u	s
SPI	s	–	s	u	s	s	u
wTVF	–	–	–	–	–	s	–
wSPI	–	–	–	–	–	–	s

stable (s), unstable (u), nonexistent (–).

The blue line with circles and the orange line with triangles denote the bifurcation thresholds for TVF and SPI, respectively, out of CCF. Filled (open) symbols indicate that the respective solution is stable (unstable) at threshold. In region E, both TVF and SPI are stable. The black solid lines describe the upper bifurcation thresholds of wTVF (■) and wSPI (♦) out of TVF and SPI, respectively. The wavy structures are stable in the respective grey coloured regions G and F and become unstable at the black dashed curve with open symbols (□, ◇). The vertical arrows (a) and (b) indicate the parameter range of the bifurcation diagrams of figure 1. The crosses denote the two parameter combinations for which the k dependence of the bifurcation behaviour is shown in figure 4. The solid violet line α in the inset divides region E into two parts: E_1 with SPI amplitudes $|u_{1,\pm 1}|$ larger than TVF amplitudes $|u_{0,1}|$ and vice versa for E_2. The dot-dashed violet curve β describes the projection of the 'bicritical' curve, i.e. the intersection line of the TVF and SPI bifurcation surfaces in (k, R_2, R_1) phase space onto the (R_2, R_1) plane at $k = 3.927$. The thick violet point denotes the 'bicritical' point γ for this k.

3.2. (R_2, R_1) phase diagram

Figure 3 exhibits a more detailed version of the phase diagram—an earlier version of which has been presented in figure 2 of [14]. It covers the whole (R_2, R_1) parameter range

investigated here. The bifurcation diagrams of figure 1 were obtained along the arrows labelled by (a) and (b).

The blue (orange) line denotes the well-known primary bifurcation threshold for TVF (SPI) out of the basic CCF state. The upper boundaries of regions F and G are the thresholds for forward bifurcations of wTVF out of TVF and of wSPI out of SPI, respectively. We found both wavy structures only as stable solutions within the parameter range investigated here. In its current form, our code does not allow to follow unstable wTVF and wSPI solutions.

The structure of the phase diagram in figure 3 can be summarized as follows: bistable TVF and SPI occur in region E above the grey coloured domains F and G. In region C (below F) only SPI but not TVF and in region D (below G) TVF but not SPI are stable. Decreasing R_1 from region E into the grey domains, TVF transfers its stability to wTVF in G while SPI lose their stability to wSPI in F. At the lower dashed boundaries of F and G, there are transients to the remaining monostable SPI and TVF, respectively. The latter bifurcate out of the CCF at the bifurcation thresholds marked by the orange line with triangles and the blue line with circles, respectively.

These bifurcation thresholds that were obtained from full nonlinear simulations with the G2D2 code differ slightly from those in figure 2 of [14] that were obtained via linear stability analysis with a shooting method; see also appendix A.

3.2.1. SPI and TVF amplitudes in region E. TVF and SPI exist as bistable solutions in region E of figure 3. However, their dominant mode amplitudes $u_{0,1}$ and $u_{1,\pm1}$, respectively, are in general different. Region E can therefore be subdivided into two subregions E_1 and E_2 by the violet α-curve in the inset of figure 3. The SPI amplitude is larger than that of TVF in E_1 and vice versa in E_2.

We would like to point out that the α-curve always lies above the upper boundary (filled lozenges) of region G. Thus, upon decreasing R_1 it is the vortex state with the smaller amplitude (TVF in E_1 and SPI in E_2) that becomes unstable against growth of waviness at the upper solid black curve of the grey regions. The state with the larger amplitude remains stable all the way down to its respective bifurcation threshold out of CCF.

3.2.2. Point of higher codimension. Within our numerical resolution, all thresholds converge in one single point of higher codimension that is marked by γ in figure 3. Therefore, direct continuous transitions between wTVF and wSPI are only possible by crossing this γ-point. Otherwise, regions F and G are separated by region E with bistable TVF and SPI. For the wavenumber $k = 3.927$ chosen here, the γ-point is given by $R_1^\gamma = 95.25$ and $R_2^\gamma = -73.69$. For other k, it moves towards higher R_1 and smaller R_2. The curve that it follows in (k, R_2, R_1) space is discussed in more detail in the following section. The projection of this curve onto the $(k = 3.927, R_2, R_1)$ plane is labelled with β in figure 3.

3.3. Wavenumber dependence

Besides the bifurcation behaviour exhibited in figure 1 as a function of R_1, we also investigated the wavenumber dependence of wavy structures for fixed R_1 and R_2. As two representative examples, we took the values marked by the crosses in figure 3.
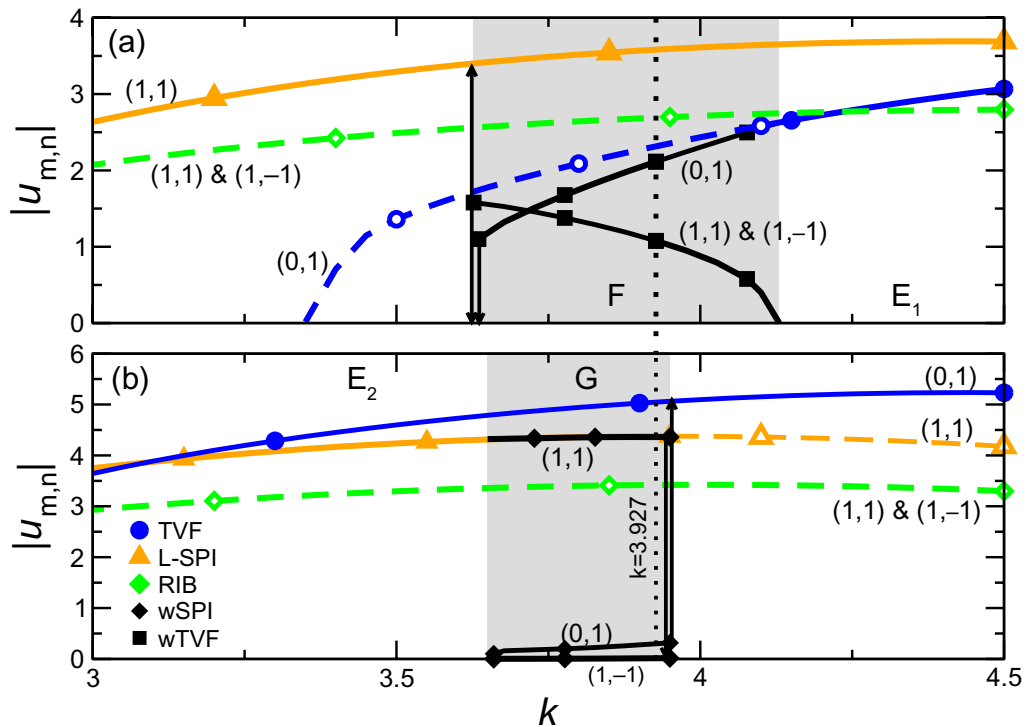
Figure 4. Bifurcation diagrams for different vortex structures versus wavenumber k. For further description cf caption of figure 1. The two parameter combinations (a) $R_1 = 120$, $R_2 = -100$ and (b) $R_1 = 96$, $R_2 = -25$ are marked by crosses in figure 3.

3.3.1. Bifurcation diagrams. Starting with a stable TVF state at $R_1 = 120$ and $R_2 = -100$ in region E of figure 4(a) and decreasing k, the TVF remains stable above the right boundary of the grey coloured area F. There, it becomes unstable against wTVF. Besides the $(0, 1)$ TVF mode, contributions of the now growing $(1, 1)$ and $(1, -1)$ modes are responsible for the azimuthal modulation of wTVF. With decreasing k and the growing contribution of the $(1, 1)$ and $(1, -1)$ amplitudes to the mode spectrum, the modulation of the wTVF becomes stronger and stronger. At the left boundary of region F, most mode amplitudes undergo a transient to zero except $(1, 1)$, which jumps up to the dominant mode of stable L-SPI as indicated by the black arrows in figure 4(a).

In the case of smaller $|R_2|$ that is shown in figure 4(b) for $R_1 = 96$ and $R_2 = -25$, the grey region G of stable wSPI lies *above* the bistable region E. Thus, the boundary of region F (G) in figure 3 of wTVF (wSPI) moves downwards (upwards) with increasing wavenumber. In that respect, it is helpful to use the phase diagram in the (k, R_1) plane shown in figure 5 in order to visualize the shape of the different regions A–E.

3.3.2. Phase diagrams. For the outer cylinder Reynolds number $R_2 = -100$ considered here, all thresholds and stability regions are topologically equivalent to those in the (R_2, R_1) plane of figure 3. The bifurcation thresholds come together in the γ-point at $k^\gamma = 5.18$ and $R_1^\gamma = 108$. The thick violet α-curve denoting equal SPI and TVF amplitudes in region E (cf figure 3)
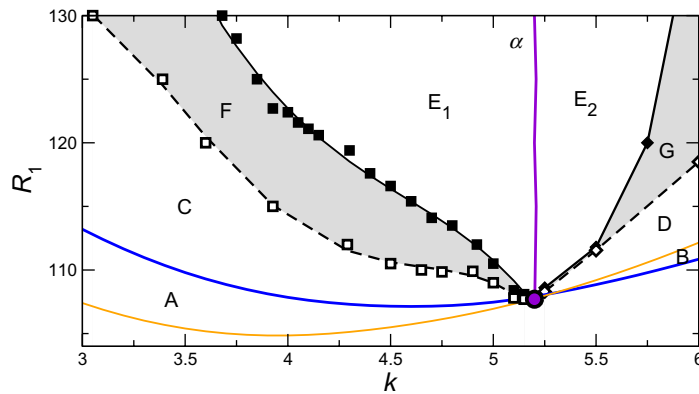
Figure 5. Phase diagram in the (k, R_1) plane for $R_2 = -100$. For a description of the regions cf figure 3.
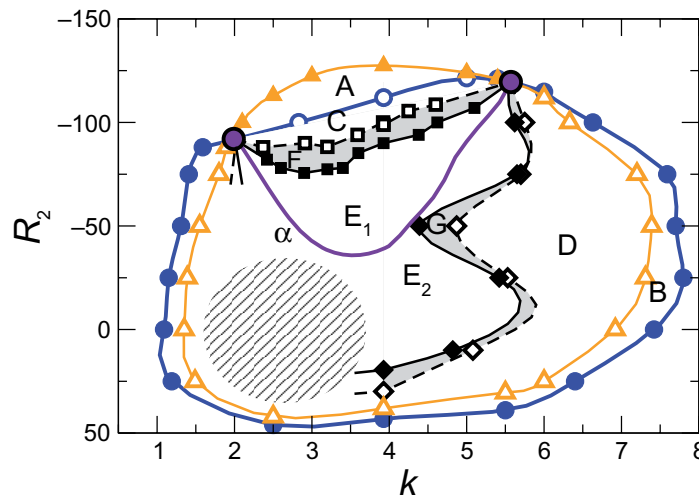

Figure 6. Phase diagram in the (k, R_2) plane for $R_1 = 115$. See figure 3 for a description of the regions and the bifurcation thresholds. The solid thick violet line represents the α-curve subdividing region E into region E_1 and E_2; cf figure 3. In the hatched area, perturbations with larger wavenumbers destabilize the solutions with periodicity $2\pi/k$. See text for further explanations.

degenerates to a straight vertical line in figure 5. Hence, the amplitudes of TVF and SPI for $k = k^\gamma$ are equal to each other independently of R_1. However, this does not hold for other R_2 as shown later.

Finally, figure 6 gives a cross section of the three-dimensional (k, R_2, R_1) phase space at $R_1 = 115$. The lines of the bifurcation thresholds and stability boundaries are arranged somewhat like onionskins. Especially, there exist two γ-points where all curves coincide. These γ-points move together for smaller R_1. Again, the solid thick violet line represents the α-curve subdividing region E into two regions E_1 and E_2 as described in section 3. It also originates in the γ-points. In region E_2 of figure 6, TVF and SPI coexist stably such that the TVF amplitude is larger than the SPI amplitude. This region should be enclosed completely from below either by the black line with filled lozenges, i.e. the bifurcation threshold to stable wSPI in region G,
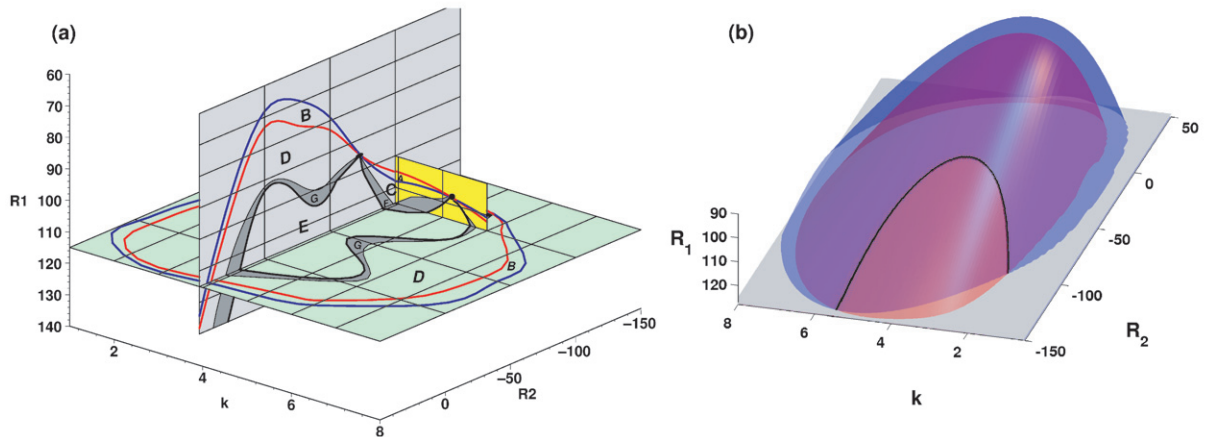
Figure 7. (a) Phase diagrams in (k, R_2, R_1) space in different sections. Phase space regions with different vortex states are identified by the lettering of figure 3. The grey section at $k = 3.927$ is shown also in figure 3, the yellow one at $R_2 = -100$ in figure 5, and the green one at $R_1 = 125$ in figure 6, respectively. (b) Neutral stability surfaces for TVF (blue) and SPI (red). The black line marks their intersection, i.e. the β-curve of the points of higher codimension.

or by the bifurcation threshold to another solution. We have indications that the two black lines delimiting region G enter indeed into the left γ-point as indicated there schematically. However, we were not able to trace out the stability boundaries of the wSPI in region G between the left γ-point at $k \simeq 2$ and the minimum at $k \simeq 4$: the hatched area in figure 6 indicates schematically that roughly in this area perturbations with larger wavenumbers prematurely destabilize the TVF and the SPI solutions.

3.4. Phase diagram in (k, R_2, R_1) space

Figure 7 provides overviews over the bifurcation surfaces and the regions where different vortex states are realized in the three-dimensional parameter space spanned by k, R_2, and R_1. Some axis directions are inverted in order to enhance the clearness and visibility of the figure. In (a), the grey section at $k = 3.927$ is shown also in figure 3, the yellow one at $R_2 = -100$ in figure 5, and the green one at $R_1 = 125$ in figure 6, respectively.

Figure 7(b) displays the two intertwined 'mountains' that are formed by the surfaces of the bifurcation thresholds for $m = 0$ TVF (blue) and $m = 1$ SPI (red) out of CCF. These surfaces were obtained by linear stability analyses of the CCF with a shooting method. The outermost surface locates the bifurcation thresholds for vortices that are stable at onset. On the other hand, the vortex solution that bifurcates from the inner one is unstable at onset.

The black line is the β-curve of the γ-points of higher codimension where the surfaces of TVF and SPI stability thresholds intersect in (k, R_2, R_1) space. The parabolic shape of the β-curve with its apex at $(k = 3.52, R_2 = -70.8, R_1 = 94.1)$ explains that for any fixed $R_1 > 94.1$, there are two γ-points and none when $R_1 < 94.1$.

Outside of the mountains in figure 7(b), the CCF state is stable so that vortices appear as solutions of the field equations only inside the mountains. The contour of these blue and red mountains can be seen in the sections of figure 7(a) as blue and red lines, respectively.

The interior of the mountains is layer-like subdivided into regions that are lettered from A to G (cf figure 3) in which different vortex states appear. The outermost layers are A (stable SPI) for small R_2 and B (stable TVF) for moderate $|R_2|$. The core of the mountain is formed by the region E of bistable TVF and SPI. In order to enhance visibility we do not show its subdivision into regions E_1 and E_2 in figure 7(a). For larger R_1, i.e. below the horizontal surfaces in figure 7, there appear, however, further instabilities [1] of TVF and SPI that are not investigated here.

4. Properties of wavy structures

Pure structures such as TVF and SPI are low dimensional in the sense that their φ- and z-dependence can be represented by only a few spatial Fourier modes. Apart from higher axial harmonics, TVF is characterized by the modes $(0, \pm 1)$. Apart from higher axial harmonics and the complex conjugates, TVF is characterized by the mode $(0, 1)$. Pure L-SPI are dominated by the $(1, 1)$ mode with higher harmonics and complex conjugates on the diagonal, $m = n$, in Fourier space. Pure R-SPI are dominated by the $(1, -1)$ mode with higher harmonics on the diagonal, $m = -n$, in Fourier space.

In contrast to SPI and TVF, wavy structures contain a mixture of these basic modes and in addition also their nonlinearly driven mode combinations.

4.1. Classification

We distinguish between vortex structures with open and closed vortices as illustrated in figure 8. There, we schematically characterize the structures by lines of constant phase that delimit the coloured stripes in figure 8 on an azimuthally unrolled cylindrical surface in the annulus. The inner squares cover one azimuthal period of 2π in the horizontal direction and one axial period of $\lambda = 2\pi/k$ in the vertical direction. For better visibility, the structures are periodically continued slightly beyond these periodicity boundaries.

Note that the lines of constant phase of the open SPI and wSPI vortices cross the horizontal boundaries, whereas those of TVF and wTVF are azimuthally closed into themselves. Generally speaking, in open left winding vortices the $(1, 1)$ mode is significantly larger than the other modes, $(0, 1)$, $(0, 2)$ and $(1, -1)$. In a pure L-SPI, the latter three modes and their complex conjugates indeed vanish. But with growing admixture of these modes the wavy modulation of the left winding spiral structure becomes stronger.

When, say, $u_{1,-1}$ has become equal to $u_{1,1}$ then one has either a RIB with $u_{0,1} = 0$ or a wTVF with $u_{0,1} \neq 0$. Note that the RIB that bifurcate as an unstable solution out of the CCF at the $m = 1$ SPI threshold are characterized by $u_{0,1} = 0$ but $u_{0,2} \neq 0$.

4.1.1. wSPI versus cross-spirals. So-called cross-spirals with azimuthal wavenumber $m = 2$ were found close to onset at different control parameters than those investigated here [15]. These patterns are basically a superposition of L- and R-SPI with different amplitudes. Similar to the wSPI considered here, these cross-spirals establish a connection between the SPI branch and the RIB branch. The latter are, however, stable at those parameters [15, 17]. The closeness to the SPI bifurcation threshold implies that the magnitude of the dominant SPI mode and of the admixture from the minority SPI mode is still small. Then, the cross-spiral state could well be explained to be basically a superposition of two $m = 2$ SPI modes, say, $(2,1)$ and $(2,-1)$ with different amplitudes.
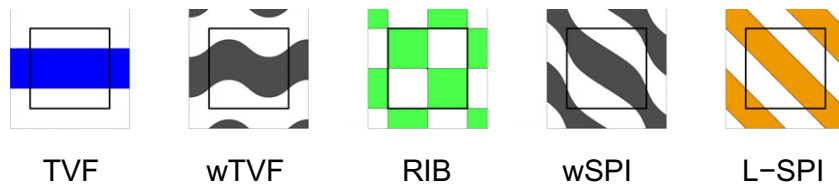
Figure 8. Schematic structure of different vortex patterns in an azimuthally unrolled cylindrical surface. In the coloured regions, the radial flow might be outwards and in the white ones inwards. The inner squares cover 2π in the horizontal direction and $\lambda = 2\pi/k$ in the vertical direction. For better visibility the structures are periodically continued slightly. The plots are obtained by superimposing contributions from the modes $u_{0,1}, u_{1,1}, u_{1,-1}$ and their complex conjugates with different weights as qualitatively shown in the table:

	$(0, 1)$	$(1, 1)$	$(1, -1)$
TVF	●	–	–
wTVF	●	◖	◖
RIB	–	●	●
wSPI	◖	●	○
L-SPI	–	●	–

The symbols denote large (●), moderate (◖), small (○) mode amplitudes and the absence (−) of a mode. The wSPI is taken here to be left winding; in its right winding mirror image the mode $(1, -1)$ would be largest.

4.1.2. wTVF occurring at large R_1. For rather moderate R_2, another regime of stable wTVF exists far beyond, say, $R_1 = 130$, i.e. beyond the driving strengths considered here. These structures are discussed, e.g. in [4, 5, 7, 18] where they are usually called WVF. From the topological as well as the bifurcation-theoretical point of view, these WVF states behave similarly to the wTVF investigated here in the sense that both bifurcate forwards out of TVF. However, WVF at large R_1 does not end in the RIB branch as our wTVF but e.g. in another wavy structure containing wavy inflow or outflow boundaries or in the same TVF branch [4, 5].

4.2. Structure of wTVF and wSPI

Structural properties of wTVF found in region F of the phase diagrams and of wSPI in region G, respectively, are illustrated in figure 9. It contains the results of numerical calculations done at (a) $R_1 = -120$, $R_2 = -100$ for wTVF and at (b) $R_1 = 96$, $R_2 = -25$ for wSPI. The top row shows isosurface plots of the azimuthal vorticity $\partial_z u - \partial_r w$. Having tested alternatives [19], we found this vorticity component to be an adequate means for visualizing shape, motion and changes of the vortex structures presented in this work.

For the parameters of figure 9, wTVF are more deformed than wSPI. The mode amplitudes of the radial velocity field in the middle row of figure 9 show that in the wTVF (a) significantly more modes are excited than in the wSPI (b). However, we also investigated other control parameters where the wSPI contained the same modes with stronger magnitudes.

The bottom part of figure 9 displays vector plots of the velocity field in the (r, z) plane.
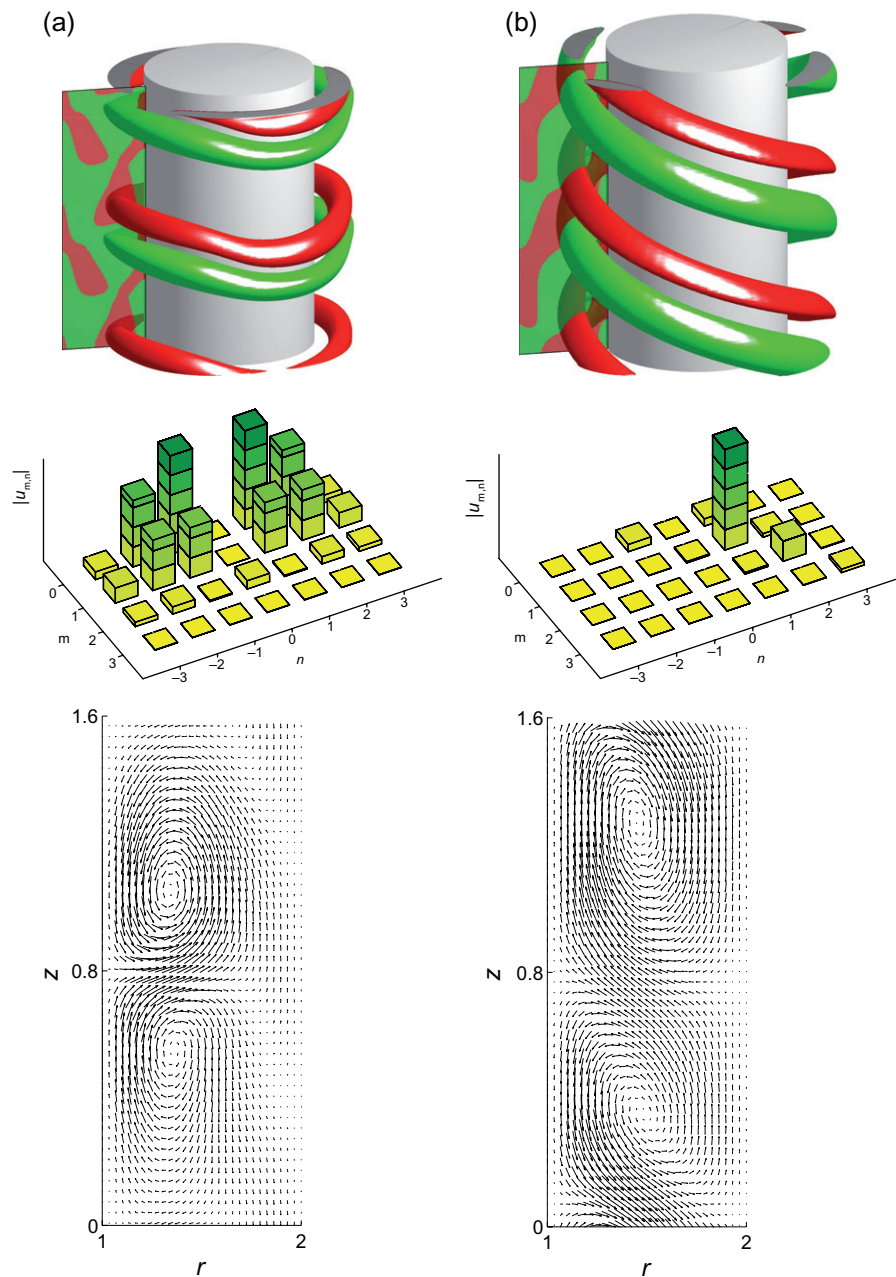
Figure 9. Structure of (a) wTVF at $R_1 = 120$, $R_2 = -100$ and of (b) left winding wSPI at $R_1 = 96$, $R_2 = -25$. Top: isosurfaces of the azimuthal vorticity $\partial_z u - \partial_r w = 70$ (red) and -70 (green), respectively. For better visibility, two periods are plotted in the axial as well as the azimuthal direction. The flat rectangular surfaces that intersect the vortices contain the sign of the azimuthal vorticity in the (r, z) plane. Middle: mode amplitudes $|u_{m,n}|$ of the radial velocity field over the (m, n) plane. Bottom: vector plots of $u(r, z)$ and $w(r, z)$ in a $\varphi = $ const plane covering one axial wavelength.
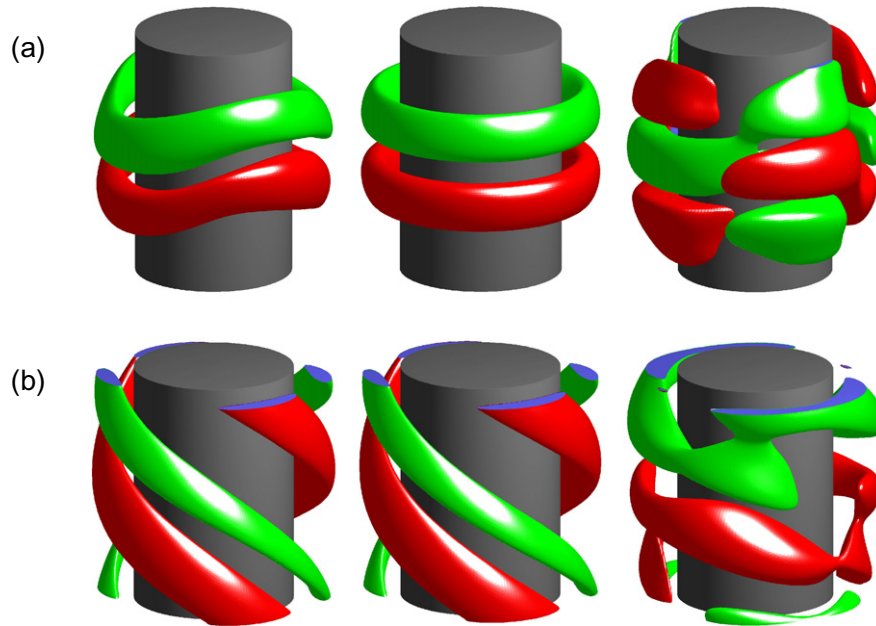
Figure 10. Isosurfaces of azimuthal vorticity $\partial_z u - \partial_r w$ of (a) wTVF at $R_1 = 120$, $R_2 = -100$, $k = 3.927$ and (b) wSPI at $R_1 = 115$, $R_2 = -50$, $k = 4.8$. The first column displays the complete structure. The second column gives the part coming for (a) from the $m = 0$ TVF mode subspace and for (b) from the $m = n$ L-SPI mode subspace, respectively. The third column gives the part resulting from the complementary rest, i.e. $m \neq 0$ (a) and $m \neq n$ (b), respectively. Red (green) indicates positive (negative) vorticity. For the sake of visibility, two periods are plotted in the azimuthal direction. The table lists the values identifying the respective vorticity isosurfaces and the respective maximal azimuthal vorticity.

	Col 1	Col 2	Col 3
(a)	60/220	60/175	15/155
(b)	90/210	90/200	6.5/25

Structural decomposition. It is interesting to elucidate the geometrical properties of wTVF and wSPI by separating the hydrodynamic fields into two parts: the first one contains only contributions from the mode subspace of the respective *pure* structure, i.e. $m = 0$ for TVF and $m = n$ for L-SPI. The second part is the rest that is generated by all modes in the respective complementary mode subspaces, i.e. $m \neq 0$ for wTVF and $m \neq n$ for a left winding wSPI.

Figure 10 shows the contributions from these two parts to the total vorticity field with the help of vorticity isosurfaces for specific values. The table lists these values together with the maximal azimuthal vorticities of the respective parts. Comparing these numbers, one sees again that the contribution from the *pure* structure's subspace dominates for the parameters chosen. In particular for the wSPI of figure 10(b), the contribution from the complementary mode subspace is very small. In general, wTVF as well as wSPI may show a broad mode spectrum depending on the control parameters. In that case, simple three mode models can be expected to be insufficient to describe the bifurcation branches.
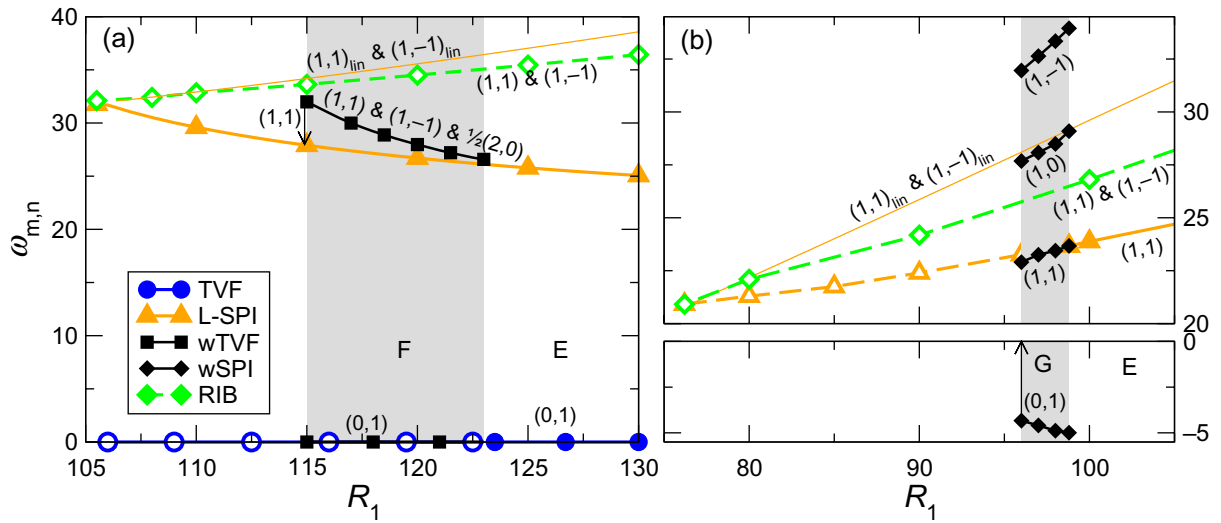
Figure 11. Bifurcation diagrams of the frequencies $\omega_{m,n}$ with which the complex mode amplitudes $u_{m,n}(r,t)$ of the radial velocity field in the middle of the gap oscillate for different vortex states with wavenumber $k = 3.927$ at $R_2 = -100$ (a) and $R_2 = -25$ (b). The corresponding bifurcation diagrams of the moduli $|u_{m,n}(r,t)|$ are shown in figure 1. Full (dashed) lines with filled (open) symbols refer to stable (unstable) solutions. Thin orange lines show linear spiral frequencies, i.e. imaginary parts of the SPI eigenvalues of the NSE linearized around the CCF state.

We finally would like to emphasize that because the isovalues are different, the plots in figure 10 give only a qualitative impression of the 'deformation' of the vorticity isosurfaces resulting from the $m \neq 0$ and $m \neq n$ mode subspace contributions, respectively.

4.3. Frequencies

Figure 11 shows the frequencies $\omega_{m,n}$ with which the complex mode amplitudes $u_{m,n}(r,t)$ of the radial velocity field, say, in the middle of the gap oscillate in the different vortex states.

SPI and RIB. Pure spirals and ribbons grow via a primary Hopf bifurcation with a common, finite frequency out of CCF. For increasing R_1, the SPI frequency increases (as in figure 11(b)) as long as $|R_2|$ is small enough [14]. For stronger counter-rotating systems, on the other hand, the spiral frequencies *decrease* with increasing R_1 (as in figure 11(a)—see also figure 3 in [14]) near onset. This is a nonlinear effect since the linear spiral frequencies, i.e. the imaginary parts of the SPI eigenvalues (thin yellow lines in figure 11) of the NSE linearized around the CCF state, increase with increasing R_1 for any R_2.

In this context, it is remarkable that the frequencies of the unstable RIB solution (green dashed lines with lozenges in figure 11) still show the same behaviour as the linear frequencies.

Wavy Taylor vortices. In the grey region F of figure 11(a), we show by the black line with squares the frequencies of wTVF for which the mode amplitudes are shown in figure 1(a). Since wTVF are time-periodic rotating states that do not propagate axially, all mode frequencies are either zero, e.g. $\omega_{0,1} = 0$, or multiples of $\omega_{1,1} = \omega_{1,-1}$. Thus, e.g. $\omega_{2,0} = 2\omega_{1,1}$. So, the dynamics of

wTVF is rather simple while the spatial structure—at least when measured by the broad mode spectrum of figure 9(a)—is complex.

It is noteworthy that our wTVF bifurcate at the right border of region F out of the TVF state with a frequency $\omega_{1,1}$ that is practically identical with the fully developed, nonlinear SPI frequency (yellow line with triangles). We have found this peculiar behaviour also for other parameters at the boundary of the grey F regions of the phase diagrams of figures 3, 5–7(a). Linear investigations by Iooss *et al* [4] do not address the issue of the wTVF frequencies at the bifurcation out of TVF. We currently have no explanation why at onset of wTVF the perturbations of $m = 0$ TVF coming from $m \neq 0$ modes with *small* amplitudes are rotated azimuthally with the same rotation frequency as the fully developed, *large*-amplitude SPI.

With decreasing R_1, the frequency $\omega_{1,1}$ of wTVF increases towards the RIB frequency. But then, at the left border of the wTVF existence region F, the frequency of the (1,1)-mode undergoes a jump down to the frequency of a pure spiral (see also figure 1(a)). The final state after the jump is either an L-SPI or an R-SPI depending on the details of the history of the system.

Wavy spiral vortices. The black lines with lozenges in figure 11(b) describe the frequencies of some of the modes that contribute to a left winding wSPI. The distribution of the mode amplitudes in Fourier space is shown in the histogram of figure 9 for the parameter combination $R_1 = 96$, $R_2 = -25$, i.e. right at the left boundary of region G in figures 1(b) and 11(b). There, by far the largest mode is (1, 1) with a frequency $\omega_{1,1} \simeq 23$ followed by the higher harmonic (2, 2). But the structurally and dynamically next important mode is (0, 1), which oscillates with a frequency $\omega_{0,1} \simeq -4.3$. The presence of these different frequencies with significant mode amplitudes makes the wSPI state quasiperiodic in time.

The spatiotemporal behaviour of such a left winding wSPI can be seen as a superposition of a major, azimuthally rotating and thereby upwards travelling wave $\propto |u_{1,1}|\cos(\varphi + kz - \omega_{1,1}t)$ and an axially downwards propagating, rotationally symmetric modulation $\propto |u_{0,1}|\cos(kz - \omega_{0,1}t)$ (cf [20]). However, for other parameters, contributions from other modes, e.g. (1, −1), can become significant. With decreasing R_1, all but (0, 1) wSPI frequencies decrease.

At the left border of region G, there occurs the transition to TVF already discussed in figure 1(b). Thus, $\omega_{0,1}$ drops to zero there as indicated by the black arrow in figure 11(b).

5. Spatiotemporal behaviour of transients

In this section, we discuss the spatiotemporal behaviour of the transformation of unstable SPI into stable TVF and of unstable TVF into stable SPI. The unstable SPI are prepared as initial states in region D of the phase diagrams in figures 3, 5, 6, and 7(a) where they coexist with monostable TVF. On the other hand, unstable TVF coexists with monostable SPI in region C of the aforementioned figures.

Preparation of unstable states. The preparation of unstable TVF and SPI as initial state was done in two different ways. One obvious way (i) was to first restrict the modes to the subspace $m = 0$ for TVF or to $m = n$ for an L-SPI, respectively, and then release this stabilizing restriction after a sufficient relaxation time in the remainder of the simulations. Another way (ii) was to judiciously use random noise as initial condition. Then, for some parameter combinations, first the unstable solution would grow before finally a transformation to the final stable state would occur. For both scenarios, we observed wavy vortices as intermediate flow during the
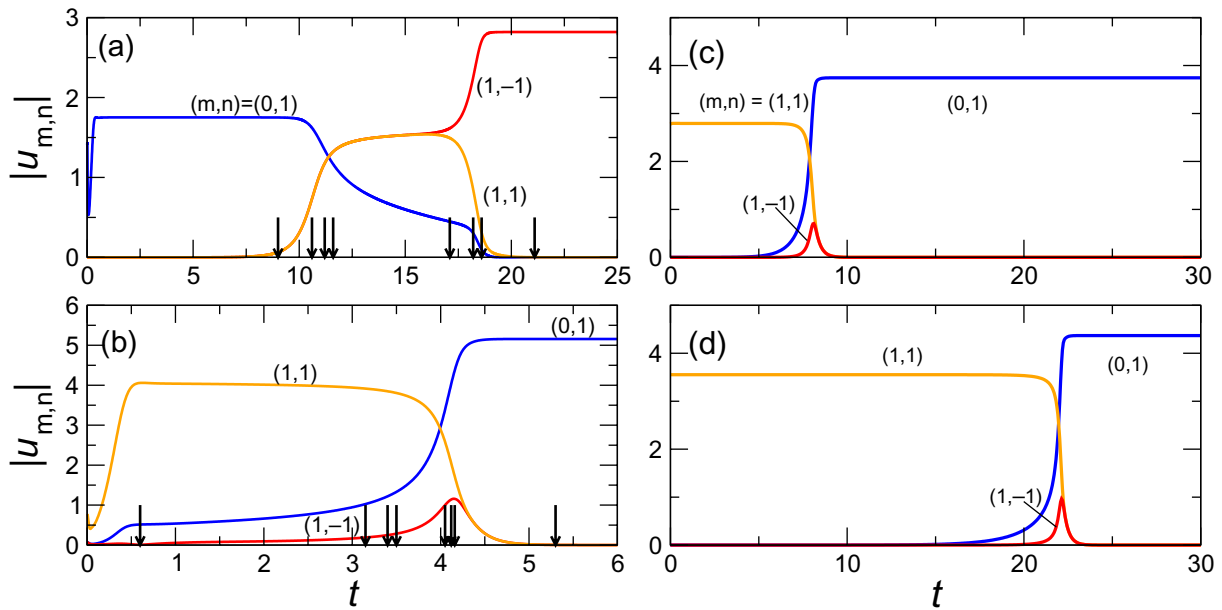
Figure 12. Time evolution of the dominant mode amplitudes $|u_{m,n}|$ during the transformation TVF $\rightarrow$ wTVF $\rightarrow$ SPI (a) and SPI $\rightarrow$ wSPI $\rightarrow$ TVF (b)–(d). Parameters for (b) $R_1 = 92.2$, $R_2 = 0$, (c) $R_1 = 85$, $R_2 = -25$ and (d) $R_1 = 90$, $R_2 = -25$ lie in region D of the phase diagrams in figures 3, 5–7(a) where SPI is unstable and TVF is monostable. For (a) the parameters $R_1 = 115$, $R_2 = -100$ lie in region C where TVF is unstable and SPI is monostable. In each case, $k = 3.927$. In (a) and (b), random noise was used as initial condition—scenario (ii), whereas in (c) and (d) the L-SPI was stabilized by mode restrictions—scenario (i). See text for further details. The arrows in (a) and (b) mark snapshot times in figure 13.

transients to the respective final states so that the transformations are TVF $\rightarrow$ wTVF $\rightarrow$ SPI and SPI $\rightarrow$ wSPI $\rightarrow$ TVF, respectively.

Time evolution of modes. Figures 12(c) and (d) depict the time evolution of the dominant mode amplitudes $|u_{m,n}|$ after the preparation scenario (i) during the transformation SPI $\rightarrow$ wSPI $\rightarrow$ TVF for two different control parameters in region D. In both cases, the system is driven away from the unstable SPI solution by computer noise only. However, the parameters ($R_1 = 90$, $R_2 = -25$) of figure 12(d) lie closer to region E where SPI are stable than the parameters ($R_1 = 85$, $R_2 = -25$) of figure 12(c). Thus, the unstable SPI in figure 12(d) survives longer than the one in figure 12(c). In both cases, there appears during a narrow time interval of about one radial diffusion time wSPI as intermediate short-lived flow.

Figures 12(a) and (b) depict the time evolution of the dominant mode amplitudes $|u_{m,n}|$ after the preparation scenario (ii). Here, simulations were done with random noise in all modes as initial conditions. The control parameters were fixed in region C ($R_1 = 115$, $R_2 = -100$ in figure 12(a)) and region D ($R_1 = 92.2$, $R_2 = 0$ in figure 12(b)), respectively. When the noise magnitude exceeds about 10^{-6} then our code generates for these parameters first the unstable solution before finally a transformation to the final stable state occurs similar to the situation

in figures 12(c) and (d). For smaller noise levels, however, the code generates immediately after having realized within about one diffusion time the unstable CCF state the *stable* final vortex state, i.e. TVF in region D and SPI in region C as one would expect considering the linear growth rates. It seems that for our parameters, larger noise forces the system faster into a nonlinear intermediate regime that favours the unstable flow before finally the stable state wins. In any case, it is quite remarkable that, e.g. in figure 12(b) at $R_2 = 0$, first the SPI and then a wSPI grows before finally TVF takes over.

Structural changes. The arrows in figures 12(a) and (b) mark the times where we made the eight snapshots of figure 13 that depict the isosurfaces of the azimuthal vorticity. They give a reasonably good impression of the structure of vortex flow. The snapshot sequences illustrate the structural changes during the transformations TVF $\rightarrow$ wTVF $\rightarrow$ SPI in figure 13(a) and SPI $\rightarrow$ wSPI $\rightarrow$ TVF in figure 13(b). Further details can be seen in the movies available from stacks.iop.org/NJP/11/053002/mmedia. Note that we use 4π cylinders in order to present the whole azimuthal variation in a single three-dimensional plot. In the axial direction, the plots cover two wavelengths.

Starting with random noise, a pure TVF state (figure 13(a1)) is established almost instantaneously on the time scale of figure 12(a). As an aside, we mention that this holds also when the initial noise distribution contains less intensity in the TVF modes than in the rest of Fourier space. With growing amplitudes of $m \neq 0$ modes the former rotational symmetric structure becomes more and more deformed, but the isovorticity surfaces are still closed in figures 13(a2)–(a3). However, the tubes formed by the isosurfaces narrow at a certain φ position. This means that the maximal vorticity within the (r, z) plane at this φ position decreases in time—the vortex intensity becomes weaker there. Note that this indentation of the vortex tubes as well as the defects rotate with the whole structure. However, this rotation intentionally cannot be seen in figure 13 due to the stroboscopic nature of the selected snapshot times.

Finally, the isosurfaces are completely constricted and separated (figures 13(a4)–(a5)). After displacing the ends of the tubes (figure 13(a6)), new connections are established in figure 13(a7) and the vorticity increases again to the final distribution in the pure R-SPI shown in figure 13(a8).

In figure 13(b), we investigate the transient SPI $\rightarrow$ wSPI $\rightarrow$ TVF for the parameter combination of figure 12(b) that lies in region D. The snapshot times are indicated by the arrows in figure 12(b). As in the case described above, we start with random noise. Now, an unstable L-SPI (figure 13(b1)) emerges first and then becomes disturbed by a growing $m = 0$ mode (figure 13(b2)). As in the above-described case, the two vortex tubes get indented and constricted, then separated, and thereafter displaced from each other (figures 13(b3)–(b5)) at a single φ position. Then the isosurfaces reconnect to form closed vortex tubes (figures 13(b6) and (b7)) and finally pure TVF in figure 13(b8).

Thus, all in all, the pairwise vortex disconnections and reconnections proceed by the generation of a pair of rotating defects at the position of minimal azimuthal vorticity.

6. Summary

We have investigated the bifurcation behaviour, dynamics and structural properties of Taylor vortices, spiral vortices, and their corresponding modulated structures, namely toroidally closed wavy Taylor vortices and helical wavy spirals as well as the so-called ribbons in the Taylor–Couette system.
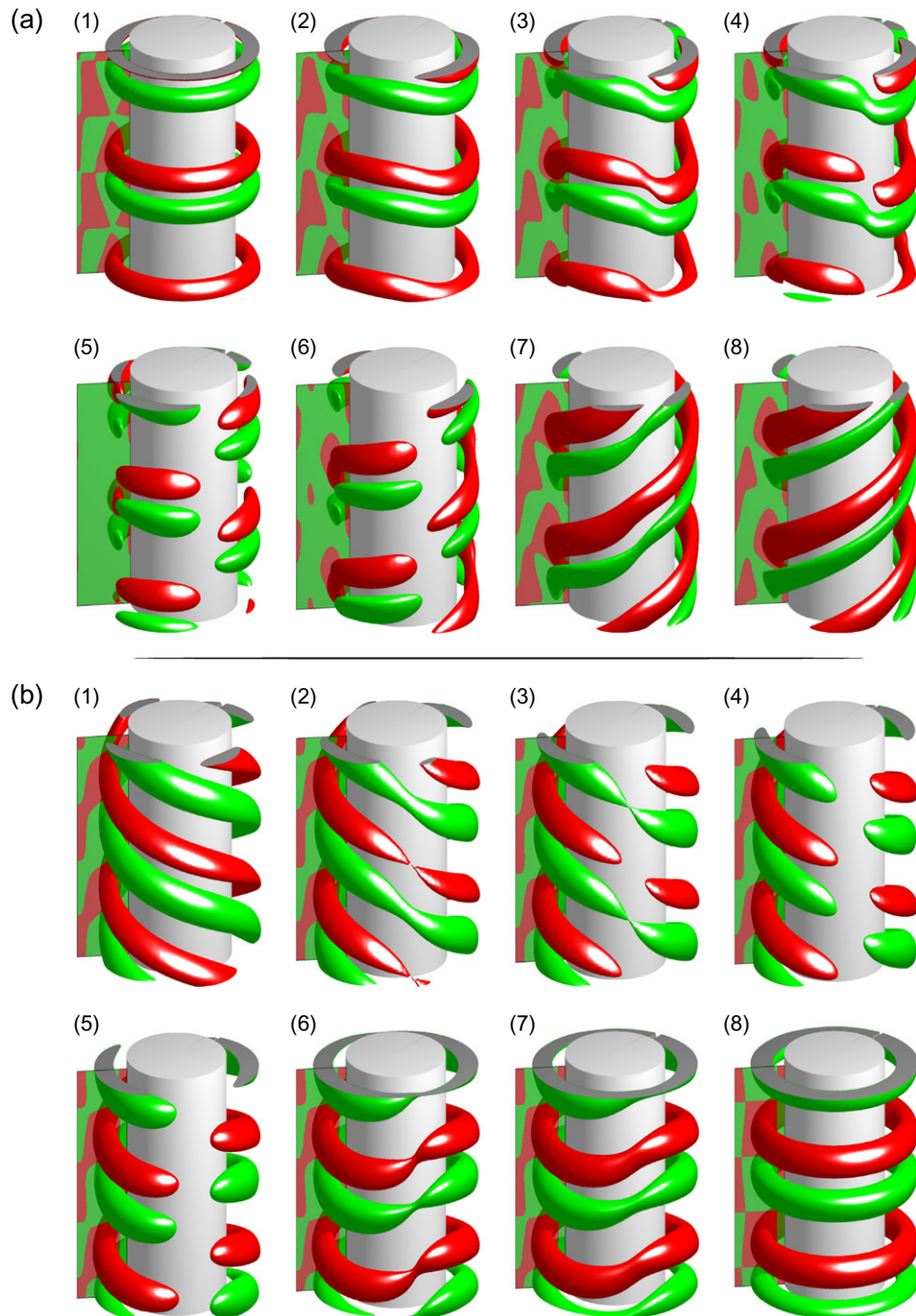
IOP Institute of Physics ⟨Φ⟩DEUTSCHE PHYSIKALISCHE GESELLSCHAFT

Figure 13. Snapshots of the isosurfaces of the azimuthal vorticity $\partial_z u - \partial_r w = \pm 60$ at eight times marked by arrows in figure 12 during the transformation (a) TVF $\rightarrow$ wTVF $\rightarrow$ SPI of figures 12(a) and (b) SPI $\rightarrow$ wSPI $\rightarrow$ TVF of figure 12(b). Red (green) colouring denotes positive (negative) vorticity. The control parameters (a) ($R_1 = 115$, $R_2 = -100$) and (b) ($R_1 = 92.2$, $R_2 = 0$) and $k = 3.927$ are those of figure 12(a) and (b), respectively. We use 4π cylinders in order to present the whole structure in a single three-dimensional plot. In the axial direction, the plots cover two wavelengths. For further details see the movies available from stacks.iop.org/NJP/11/053002/mmedia.

Under periodic axial boundary conditions, the transition from unstable TVF to stable SPI is performed by generating stable wTVF. Similarly, stable wSPI mediate the transition from unstable SPI to stable TVF. The wTVF solution branch was known already from the literature to connect the TVF with the unstable RIB state. We elucidated this connection in quantitative detail. Furthermore, we found evidence that the wSPI branch connects the SPI solution to the unstable RIB solution. Since, however, the RIB solution is unstable in both cases, the system 'jumps' to the remaining stable solution when following the wavy states to their end close to the RIB state.

This behaviour reflects the fact that in solution space (i) the parameter region F (G) of stable wTVF (wSPI) separates the region E of bistable SPI and TVF from region C (D) with monostable SPI (TVF) and that (ii) the stable wTVF (wSPI) coexist bistably with SPI (TVF) in region F (G). This holds in the complete (k, R_2, R_1) phase space. In region E, near the bifurcation threshold of wTVF out of TVF, the amplitude of TVF is larger than that of SPI and vice versa for wSPI bifurcating out of SPI. On the other hand, if one starts in the monostable region C (D) with unstable TVF (SPI) then this unstable solution decays and transforms into stable SPI (TVF). The time needed for this transient increases with decreasing distance from the region E of bistability of SPI and TVF.

The wavy structures of wTVF and wSPI 'live' in a more complex Fourier subspace with more nonzero Fourier modes than for the pure structures of TVF and SPI. However, there are spatiotemporal restrictions; in the case of the axially nonpropagating and temporally periodic wTVF solution, the $(1, 1)$ mode is equal to the $(1, -1)$ mode. In the case of the temporally quasi-periodic left winding wSPI solution the main $(1,1)$ mode contributes to an azimuthal rotation and axial propagation of the whole structure with a frequency $\omega_{1,1}$ that differs from the frequency $\omega_{0,1}$ with which a rotationally symmetric modulation wave is propagating axially downwards.

Concerning the frequency of wTVF, we made the puzzling and unexplained observation that the infinitesimal $(1, \pm 1)$ wavy perturbations of TVF at the onset of wTVF are azimuthally rotated with the same frequency as the large-amplitude $(1, \pm 1)$ modes in the nonlinear SPI that coexist bistably with TVF and wTVF there.

The wavenumber dependence of the wavy structures is similar to that of the pure ones. All structures investigated here lie in the three-dimensional (k, R_2, R_1) phase space inside a volume that is bounded by two intertwined surfaces over the (k, R_2) plane. The two surfaces are the bifurcation thresholds of TVF and SPI, respectively. At their intersection curve also the other bifurcation thresholds of wTVF, wSPI, and RIB come together.

We analysed the spatiotemporal changes in the flow during the transformation from unstable TVF to stable SPI in region C and from unstable SPI to stable TVF in region D. Using among others, a flow visualization with isosurfaces of the azimuthal vorticity, we could follow in detail how the closed vortex tubes of TVF are constricted and broken up in pairs of rotating defects and how then the tube ends move axially apart and reconnect to generate the helicoidal vortex tubes of the SPI. The transformation from SPI vortex tubes to closed TVF tubes proceeds in an almost inverse manner to the above-described scenario containing also constriction, disconnection, separation and finally reconnection of the tubes.
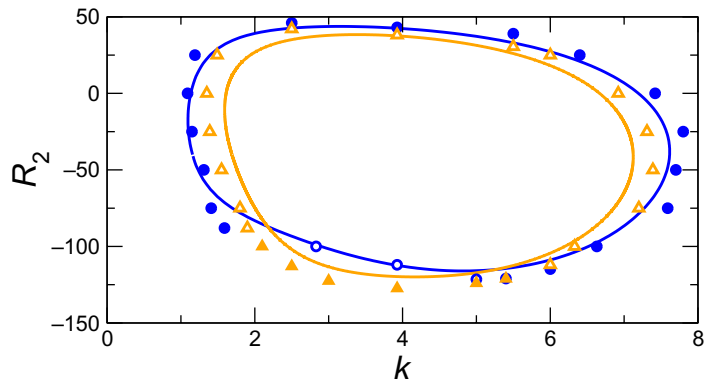
Figure A.1. Comparison of the bifurcation thresholds in the (k, R_2) plane at $R_1 = 115$ computed by G2D2 (symbols) with the linear stability boundaries of CCF against TVF (blue curve) and SPI (orange curve) perturbations. Open (closed) symbols denote bifurcation thresholds of unstable (stable) solutions.

Table A.1. Averaged value $E(\cdot)$ and standard deviation $\sigma(\cdot)$ of the relative errors $\delta k = |k_{G2D2}/k_{lin}| - 1$ and $\delta R_2 = |R_{2,G2D2}/R_{2,lin}| - 1$ in k and R_2 taken from the bifurcation thresholds of figure A.1.

	$E(\delta k)$	$\sigma(\delta k)$	$E(\delta R_2)$	$\sigma(\delta R_2)$
TVF	0.034	0.039	0.09	0.20
SPI	0.053	0.050	0.15	0.29

Appendix A. Numerical method

We used both codes, G2D2 and G1D3, as mentioned in section 2. The advantages of G2D2 are that with decomposition (4) of the fields, one can easily restrict the set of modes in order to enforce symmetries and that it is faster than G1D3.

For our calculations we chose time steps complying with the diffusive von Neumann condition as well as with the advective Courant–Friedrichs–Levy condition. We found $m_{max} = n_{max} = 4$ in combination with a radial discretization interval of $\Delta r = 0.05$ and time steps of $\Delta t \approx 0.0005$ to be sufficiently accurate. Several control runs with $m_{max} = n_{max} = 8$ and $\Delta t < 0.0005$ did not show appreciable differences in the parameter range investigated here. All in all, we found that G2D2 yields slightly different amplitudes than G1D3 and better accuracy concerning the bifurcation thresholds.

To convey an idea of the accuracy of the G2D2 code, we compare in figure A.1 the bifurcation thresholds of TVF (blue) and SPI (orange) obtained by a shooting method [21] (solid lines) from the linearized NSE with those obtained by extrapolating nonlinear G2D2 amplitudes to zero (symbols) for $R_1 = 115$ as a representative example.

We found the numerical errors of G2D2 relative to the shooting results to be comparable with those of G1D3. Table A.1 gives averaged relative errors and their standard deviations for both methods.

IOP Institute of Physics ΦDEUTSCHE PHYSIKALISCHE GESELLSCHAFT

References

[1] Tagg R 1994 *Nonlinear Sci. Today* **4** 1
[2] Golubitsky M, Stewart I and Schaeffer D 1988 *Singularities and Groups in Bifurcation Theory* vol II (New York: Springer)
[3] Golubitsky M and Langford W F 1988 *Physica* D **32** 362
[4] Iooss G 1986 *J. Fluid Mech.* **173** 273
[5] Jones C A 1984 *J. Fluid Mech.* **157** 135
[6] Tagg R, Hirst D and Swinney H L, unpublished
[7] Andereck C D, Liu S S and Swinney H L 1986 *J. Fluid Mech.* **164** 155
[8] Antonijoan J and Sanchez J 2000 *Phys. Fluids* **12** 3147
[9] Antonijoan J and Sanchez J 2002 *Phys. Fluids* **14** 1661
[10] Demay Y and Iooss G 1984 *J. Mech. Theor. Appl. Spec. Suppl.* 193
[11] Chossat P and Iooss G 1994 *The Couette–Taylor Problem* (New York: Springer)
[12] Ahlers G, Cannell D S and Dominguez Lerma M A 1983 *Phys. Rev.* A **27** 1225
[13] Park K 1984 *Phys. Rev.* A **29** 3458
[14] Hoffmann Ch, Lücke M and Pinter A 2004 *Phys. Rev.* E **69** 056309
     Hoffmann Ch, Lücke M and Pinter A 2006 *Phys. Rev.* E **74** 049901 (erratum)
[15] Pinter A, Lücke M and Hoffmann Ch 2006 *Phys. Rev. Lett.* **96** 044506
[16] Hoffmann Ch and Lücke M 2000 *Physics of Rotating Fluids* (Berlin: Springer) pp 55–66
[17] Pinter A, Lücke M and Hoffmann Ch 2007 *Phys. Rev.* E **76** 015301
[18] Jones C A 1981 *J. Fluid Mech.* **102** 249
[19] Chakraborty P, Balachandar S and Adrian R 2005 *J. Fluid Mech.* **535** 189
[20] Pinter A, Lücke M and Hoffmann Ch 2008 *Phys. Rev.* E **78** 017303
[21] Pinter A, Lücke M and Hoffmann Ch 2003 *Phys. Rev.* E **67** 026318